Liquid exfoliation of $Ni_2P_2S_6$: Structural characterisation, size-dependent properties and degradation

Kevin Synnatschke,[1] Shouqi Shao,[2] Jonas van Dinter,[3] Yvonne J. Hofstetter,[4,5] Daniel James Kelly,[2] Sebastian Grieger,[1] Sarah J. Haigh,[2] Yana Vaynzof,[4,5] Wolfgang Bensch,[3] Claudia Backes,[1*]

[1]*Institute for Physical Chemistry, Heidelberg University, D-69120 Heidelberg, Germany*

[2] *School of Materials, University of Manchester, Oxford Road, Manchester M13 9PL, United Kingdom*

[3] *Institute of Inorganic Chemistry, University of Kiel, Max-Eyth-Straße 2, 24118 Kiel, Germany*

[4] *Kirchhoff-Institute for Physics, Heidelberg University, Im Neuenheimer Feld 227, 69120 Heidelberg*

[5] *Centre for Advanced Materials, Heidelberg University, Im Neuenheimer Feld 225, 69120 Heidelberg, Germany*

* backes@uni-heidelberg.de

Abstract:

Reducing the size of a material, from a bulk solid to a nanomaterial, may lead to drastic changes of various properties including reactivity and optical properties. Chemical reactivity is often increased due to the nanomaterial's higher effective surface area, while confinement and geometric effects lead to systematic changes in optical properties. Here, we investigate the size-dependent properties of $Ni_2P_2S_6$ nanosheets that were obtained from liquid phase exfoliation in *N*-cyclohexyl-2-pyrrolidone. The as-obtained stock dispersion was size-selected by liquid cascade centrifugation resulting in fractions with distinct size and thickness distributions, as quantified by statistical atomic force microscopy. Raman, TEM, XRD and XPS characterisation revealed the exfoliated flakes have good crystallinity and high structural integrity across all sizes. The optical extinction and absorbance spectra systematically change with the lateral dimensions and layer number, respectively. Linking these changes to nanosheet dimensions, allows us to establish quantitative metrics for size and thickness from optical properties. To gain insights in to the environmental stability, extinction/absorbance behaviour was followed as a function of time at different storage temperatures. Degradation is observed following first-order kinetics and activation energies were extracted from the temperature dependent data. The decomposition is due to oxidation which appears to occur both at edges and on the basal plane.

Introduction:

Synthesis of layered transition metal hexathiohypo diphosphates was first reported in 1894[1] and described in more detail about 50 years ago.[2] A great strength of this class of materials is the structural variety that gives rise to a whole host of interesting electronic and magnetic properties.[3] In recent years, they have been extensively investigated in electrochemical energy storage and conversion.[4] For example, a comparative study of ten different transition metal hexathiohypo diphosphates revealed that $Ni_2P_2S_6$ and $Co_2P_2S_6$ exhibit superior performance in the hydrogen evolution reaction (HER), while $Mn_2P_2S_6$ has the highest activity in the oxygen reduction reaction (ORR) and $Co_2P_2S_6$ in the oxygen evolution reaction (OER).[5]

$Ni_2P_2S_6$ is a particularly interesting member of this class of materials, exhibiting a large storage capacity for Li^+ ions, with $Li_xNi_2P_2S_6$ where x is well above one, found for bulk crystals.[6] The bulk material has demonstrated high potential as an anode material in energy applications already in 1979.[7] The electrochemical performance is expected to further improve if the active surface area of the material could be increased by employing nanostructured $Ni_2P_2S_6$ rather than the bulk solid. For example, GaS and V_2O_5 have both shown improved long-term stability and storage capacity by using nanosheets rather than the corresponding bulk materials.[8, 9] Similarly, nanosheets of $Ni_2P_2S_6$ have shown an improved performance over the bulk material in lithium ion storage[10] as well as in electrocatalysis for both OER[10] and HER.[11] In particular, a stable performance over a wide range of pH was observed for the hydrogen evolution reaction.[11]

Increased active surface area can generally be achieved by a broad palette of methods such as controlled growth[12] or via mechanical methods such as high energy milling or liquid-phase exfoliation (LPE) techniques.[13, 14] While each method has its respective advantages and disadvantages, liquid exfoliation has gained increasing importance over the past decade. This is because the process is very versatile, scalable and applicable to a large variety of layered crystals resulting in the production of colloidally dispersed nanosheets that can be conveniently processed into thin films or blended with other materials in composites.[14, 15] Examples of layered materials that have been exfoliated include graphite,[16, 17] *h*-BN,[18, 19] transition metal dichalcogenides (TMDs),[20, 21] transition metal oxides,[22, 23] black phosphorous (BP),[24, 25] layered III-VI semiconductors (e.g. GaS,[26] InSe[27]), IV-VI semiconductors (e.g. SnS,[28] GeTe[29]), hydroxides (e.g. $Ni(OH)_2$[30] or $Co(OH)_2$[31]), layered silicates[32] among others. The method is based on immersing the samples into a suitable solvent and using shear- or ultrasonic energy to overcome the relatively weak interlayer forces and exfoliate the crystal into two dimensional sheets. Once exfoliated, the solvent or stabiliser prevents the nanomaterial from reaggregation by occupying the sheet surfaces. The use of appropriate solvents (matching the surface energies of solvent and solute)[17, 33] or surfactants[16, 34] is crucial in order to produce a stable dispersion with achievable concentrations up to several g/L. The main disadvantage of LPE is the polydispersity in the lateral sizes and thicknesses of the nanosheets that are obtained. To this end, size selection techniques,[35] for example by liquid cascade centrifugation (LCC)[36] have

been established. Since the dimensions of nanosheets dramatically influence their properties, size selection is crucial for using LPE nanosheets- both for fundamental and applied studies.

Recently, it was demonstrated that LPE can also be applied to layered $Ni_2P_2S_6$ crystals.[10] However, in the previous work, no size selection and statistical size/thickness quantification was performed so that it is currently unclear what nanosheet size and thicknesses can conveniently be produced. In addition, size-dependent optical properties have not been reported. In particular for LPE nanosheets, these have shown to be powerful as they can be used to assess nanosheet dimensions spectroscopically.[26, 36, 37] Furthermore, it is currently unclear whether exfoliated $Ni_2P_2S_6$ is stable under ambient conditions or whether it oxidizes similar to other materials such as black phosphorus,[24, 38, 39] TiS_2[40] or MoO_2.[23] This information is absolutely crucial giving the interest in using transition metal hexathiohypo diphosphates as catalysts for water splitting.[4]

Here, we address these points. We use LCC to produce colloidally stable dispersions of $Ni_2P_2S_6$ with different nanosheet size and thickness ranges. The nanosheet dimensions were quantified by statistical atomic force microscopy measurements. This allows us to quantitatively link size-dependent changes in optical extinction and absorbance spectra to nanosheet size and thickness resulting in readily accessible spectroscopic metrics. In addition, the environmental stability of exfoliated $Ni_2P_2S_6$ is assessed by following the absorbance and extinction behaviour as a function of time at different storage temperatures to determine an average activation energy for the degradation.

Results and Discussion

Characterisation of the bulk material

$Ni_2P_2S_6$ bulk material was synthesised via a high temperature solid state reaction as reported previously by Rao et al.[41] Prior to exfoliation, the bulk material (for structure see Figure 1A) was characterised by scanning electron microscopy (SEM), energy-dispersive X-ray spectroscopy (EDX), X-ray photoelectron spectroscopy (XPS), X-ray powder diffraction (XRD) and Raman spectroscopy. SEM (Figure 1B) confirms the layered character with crystallites having dimensions of several μm. The chemical composition is both confirmed by EDX and XPS. The EDX spectrum is dominated by the $Ni_{L\alpha}$, $P_{K\alpha}$ and $S_{K\alpha}$ lines (Figure 1C) yielding a stoichiometry of $NiPS_{2.9}$. This is confirmed via XPS which gives a stoichiometry of $Ni_{0.76}PS_3$. The XPS S 2p (Figure 1D) and P 2p (Figure 1E) regions show the characteristic $2p_{1/2}$-$2p_{3/2}$ doublets with no traces from oxides or other phases. The binding energies of 165 eV (S $2p_{3/2}$) and 132 eV (P $2p_{3/2}$) are typical for the oxidation states S^{2-} and P^{4+}. The high purity and crystallinity of the sample is obvious from the XRD pattern, and the reflection positions match a calculated diffractogram from literature data (Figure 1F). The experimental pattern exhibits slightly different intensity ratios, which is caused by preferred orientation of the crystallites, a phenomenon well documented for layered materials.[42-45] Because X-ray diffraction is not very

sensitive to minute impurities, the presence of tiny amounts of a second phase cannot be excluded.

The Raman spectra show the characteristic lattice vibrations of hexathiohypo diphosphates (Figure 1G) and are in agreement with literature.[46] The same modes are observed for 532 nm and 633 nm excitation with only minor effects from changing the resonance conditions. For example, the relative intensity of $A_{1g}^{(1)}$ is increased at 633 nm excitation compared to the excitation with 532 nm. Overall, the $Ni_2P_2S_6$ starting material was found to have high purity and structural integrity.

Exfoliation and size selection

For liquid-phase exfoliation, the $Ni_2P_2S_6$ bulk material was immersed into *N*-cyclohexyl-2-pyrrolidone (CHP) and subjected to tip sonication (see methods). Pyrrolidone-based solvents such as CHP or *N*-methyl-2-pyrrolidone (NMP) are known to be efficient solvents for LPE for a range of layered crystals[14], preventing nanosheet reaggregation after exfoliation. In addition, potential degradation due to chemical reactions with water and air can be supressed as demonstrated for black phosphorous[24] and TiS_2.[40]

Dispersions obtained by LPE are intrinsically polydisperse, containing nanosheets with broad size and thickness distributions. To gain insights into size-dependent properties, a method for size selection is required. Various methods have been established,[35] ranging from density gradient ultracentrifugation (DGU), which allows a precise size control of the obtained nanosheets at low yields, to liquid cascade centrifugation (LCC), which gives poorer control over size and thickness of the nanosheets, but yields a larger amount of material. In contrast to DGU, LCC can be readily applied to a range of nanosheet dispersion in solvents with little fine-tuning required.

The stock dispersion of exfoliated $Ni_2P_2S_6$ in CHP is subjected to a standard LCC protocol (see methods section for details) of consecutive centrifugation steps with increasing accelerations (expressed in relative centrifugal force, RCF, as multiples of the earth's gravitational acceleration, g) as introduced previously.[36] In brief, the stock dispersion is first centrifuged at low centrifugal acceleration and unexfoliated material is removed. The supernatant is carefully decanted and centrifuged at slightly higher centrifugal acceleration. Again, supernatant and sediment are separated. The sediment is collected in fresh solvent of reduced volume and the supernatant centrifuged at even higher centrifugal acceleration. This procedure is repeated with iteratively increasing centrifugal accelerations. After each step, the sediment is separated from the supernatant and analysed, while the supernatant is used for the subsequent step. The final supernatant is discarded. As the nanosheet dispersion progresses through the cascade, smaller and smaller nanosheets are collected in the sediment with increasing centrifugal acceleration. Importantly, redispersion of the sediment allows reduction of the dispersion volume and an increase in the nanosheet concentration to facilitate further

analysis. In this work, two cascades with slightly different centrifugation boundaries are tested to verify the robustness of the size selection. We therefore label the size-selected dispersions by the lower and the upper centrifugal acceleration used for material sedimentation (see methods section for a detailed description).

To determine the nanosheet dimensions, the high concentration CHP dispersions obtained after LCC were diluted with isopropanol, drop-cast onto Si/SiO_2 wafers and subjected to atomic force microscopy (AFM) characterisation. Representative wide field images for each size fraction are shown in the SI and confirm the presence of nanosheets in all cases. Care must be taken when analysing the AFM height measurements of the objects since the apparent thickness of LPE nanosheets is typically overestimated compared to the theoretical thickness due to additional contribution from residual solvent, measuring parameters (e.g. measurement setpoint, free amplitude, etc.) and chemical characteristics of the surface.[47, 48] This means an apparent height, which is proportional, but not identical to the real height, is measured. In order to determine the measured apparent AFM thickness of one layer, step height analysis can be performed.[19, 24, 29, 37] In this approach, line profiles across the terraces of incompletely exfoliated nanosheets are extracted as exemplarily shown in figure 2A. These are sorted by the measured height in ascending order in figure 2B. Discrete steps with a height of 1.5 nm are observed which is assigned to the apparent AFM thickness of one layer of LPE $Ni_2P_2S_6$. Hence, to convert the AFM height data to layer number, the measured height is divided by 1.5 nm, i.e. a factor of 2.3 larger than the interlayer spacing of 0.65 nm.

The dimensions of the nanosheets in each size-selected fraction were analysed statistically via the longest dimension (nanosheet length, L) and the sheet height recorded for ~200 individually deposited nanosheets. The nanosheet height was converted to layer number, N, with aid of the step height analysis described above. The lateral dimensions were corrected for cantilever broadening and pixilation effects.[49] After such corrections, distribution histograms of L (Figure 2C,D) and N (Figure 2E,F) are obtained as exemplarily shown for a fraction enriched in larger (Figure 2C,E) and smaller (Figure 2D,F) nanosheets respectively. For all data, see SI Figure S1 and S2. The insets in Figure 2C,D show typical nanosheets representative of the respective dispersion. The distribution in each fraction follows a log-normal distribution for all nanosheet dimensions, <L> and <N>, as previously observed for other materials.[50, 51]

To investigate the results of the centrifugation cascade, the arithmetic mean values of length, <L> and layer number, <N> are plotted as a function of the midpoint of the pair of the centrifugation boundaries used between the two centrifugation steps (central RCF) in figure 2G,H, respectively. <N> and <L> both decrease as a power law, as indicated by the dashed lines with increasing centrifugation speed as observed previously.[36, 52] Fitting the data results in an exponent of 0.21 in case of <L> and 0.23 in case of <N>. The datapoints from both cascades fall on the same curve. <L> ranges from ~100-350 nm, while <N> ranges from ~5-17

layers. The arithmetic mean of the lateral size and layer numbers for each fraction is shown in table 1 in addition to the yield which was determined gravimetrically (see methods). Note that the overall yield of exfoliated nanosheets depends on the lower centrifugation boundary cut-off where the unexfoliated material is removed. When an RCF of 100 *g* is chosen, the overall yield is ~30 %. While this corresponds to a relatively low production rate of 3 mg/h., we note that this is due to the low initial mass of 50 mg bulk material per exfoliation run. The yield is in fact similar to graphene produced by sonication-assisted LPE[53] so that we anticipate that similar production rates as with graphene can be achieved when optimising the exfoliation process.

Structural characterisation of the nanosheets.

For characterisation of the structural integrity of nanosheets, size-selected fractions were subjected to a range of characterisation techniques. Different fractions of the size-selected nanomaterial (0.6-3k *g*, 3-10k *g* and 10-50k *g*) were united in order to probe a sufficient amount of material and analysed via XRD (dispersed in CHP) to check for structural changes compared to the bulk crystal (Figure 3A). Prior to the XRD measurement, the dispersion was sonicated for 10 min. in an ultrasonic bath to redisperse aggregated particles. The comparison of the patterns of the bulk sample and of the exfoliated material suggests that $Ni_2P_2S_6$ is not destroyed during the exfoliation process, as the Bragg reflections characteristic of bulk $Ni_2P_2S_6$ can be observed in the pattern from the exfoliated samples. However, the (001) reflection clearly exhibits less intensity in the pattern of the exfoliated samples and the (002) reflection disappeared completely after the exfoliation process. This decrease in intensity of these two Bragg peaks is expected to result from exfoliation of the (001) basal planes and the lower number of atomic layers per particle, as the layers of $Ni_2P_2S_6$ are stacked along [001].

Raman measurements with a 532 nm excitation laser were conducted on drop-cast samples from the different fractions (the small fraction is 5-30k *g*, the large one is 0.1-0.4k *g*, Figure 3 B, additional sizes: see SI Figures S1 and S2). The spectra show the same vibrational modes observed for the bulk crystals and are in good agreement with expected literature data.[46] No significant variation across the different fractions is observed. Further characterisation of the nanosheets was done by transmission electron microscopy (TEM). Nanosheets of similar morphology to AFM images are observed (Figure 3 C and SI Figures S4 A-C). The selected area electron diffraction pattern (SAED) of the nanosheets (inset) found in the fraction isolated at low centrifugal acceleration (0.1-0.4k *g*) shows sharp and bright diffraction spots consistent with the expected pattern for single crystal $Ni_2P_2S_6$ material (Figure 3D). Similar results were observed for smaller nanosheets isolated at higher centrifugal acceleration (see SI Figure S4 C,F). In some cases, diffraction patterns consistent with polycrystalline material are observed (see SI Figure S4 G,J), which is attributed to randomly restacked or several rotated nanosheets within the ~100 nm diameter SAED field of view.

High-resolution TEM (HRTEM) imaging of the $Ni_2P_2S_6$ basal planes reveals the expected atomic lattice as exemplarily shown for the 0.1-0.4k g fraction in (Figure 3 E, F; more examples, see SI Figure S4). Lattice spacing is found at 4.98 Å, 4.86 Å, 4.86 Å and 2.85 Å corresponding to the expected (020), (110), $(\bar{1}10)$ and $(\bar{1}30)$ crystal planes of $Ni_2P_2S_6$. In addition, STEM-EDX maps were measured of freshly-prepared nanosheets from the small-sized (3-10k g) fraction, revealing a uniform distribution of the different elements with a stoichiometry of $NiPS_{2.8}$ (see SI, Figure S5).

Size-selected fractions were subjected to XPS after filtration. S 2p and P 2p core level spectra of the fraction isolated at low (0.1-0.4k g, denoted as large) and high centrifugal acceleration (5-30k g, denoted as small) are exemplarily shown in figure 3G-H (additional data see SI, Figures S6 and S7). In particular for small nanosheets, additional doublets are observed at higher binding energy consistent with oxidised sulfur (Figure 3G) and phosphorous (Figure 3H). The degree of oxidation scales best with the mean nanosheet volume and not length or thickness, (see SI Figure S8) suggesting a size-independent degradation of the material. The different degrees of oxidation are attributed to larger surface area in the case of smaller/thinner nanosheets. Interestingly, oxidation is more pronounced at phosphorous sites (reaching up to 25 %) than at sulfur sites (< 5 %), which is presumably due to the higher oxophilicity of phosphorous compared to sulfur or due to dissolution of oxidised sulfur.

The stock dispersion prior to LCC was also subjected to XPS, in addition to the size-selected fractions, and shows a much larger contribution from oxidised species (up to 58 %, see SI, Figure S7). This highlights that LCC not only leads to size selection, but also to purification of the nanomaterial, as soluble impurities as well as highly defective/small nanosheets are discarded with the supernatant after the last step of the cascade. Overall, structural characterisation of the nanosheets demonstrates that they are widely intact after LPE and remain highly crystalline with only minor surface oxidation, which is addressed further below.

Size-dependent optical properties.

As demonstrated for a range of 2D materials,[19, 24, 26, 36, 37] optical extinction and absorbance spectra change with material dimensions. Knowledge of nanosheet size and thickness from AFM allows quantitative investigation of these changes in $Ni_2P_2S_6$ nanosheets (Figure 4). Optical extinction and absorption spectroscopy is used in transmission mode, where $T = 10^{-Ext}$ with $Ext = \varepsilon \cdot c \cdot d$ (ε = extinction coefficient, c = concentration of the nanosheets and d = depth of the light path). It should be emphasized that the extinction (Ext) is a combination of absorption (Abs) and scattering ($Scat$), where $Ext(\lambda) = Abs(\lambda) + Scat(\lambda)$.[37, 54, 55]

The spectra in figure 4A show the extinction coefficients as a function of wavelength, calculated from gravimetric mass determination (see methods) for the different size-selected fractions of the first cascade (for the 2nd cascade data see SI Figures S9-10). The optical spectra clearly change with the increasing size of the material as indicated by the arrow. It was also demonstrated for other materials that both, lateral size and layer number are of major impact on the spectral shape and thus the extinction/absorbance coefficient.[19, 24, 26, 36, 37] One effect of changing the nanosheet dimensions is that scattering contributes differently to the extinction spectra. This is typically described by a power law decrease in the extinction at long wavelengths in the non-resonant regime[54] and such behaviour can be observed in the $Ni_2P_2S_6$ extinction coefficient spectra (Figure 4A).

To further investigate the optical properties, the dispersions were measured in the centre of an integrating sphere, where the scattered light is collected to determine the absorption coefficient spectra (Figure 4B, see methods). The difference is best illustrated by a direct comparison of optical extinction, absorbance and scattering coefficient spectra (Figure 4B, inset or SI Figure S9). It is clear that light scattering is non-negligible in these dispersions but to fully understand the optical response, the absorbance spectra must be analysed in more detail. Note that, in contrast to extinction, the absorbance of all fractions approaches zero at long wavelengths, indicating an optical band gap at ~875 nm (1.42 eV), which shifts towards ~825 nm (i.e. a larger gap of 1.50 eV) for increasing centrifugal force and thus smaller particles. Similar to extinction, differences in the absorbance coefficients across the samples in the resonant regime can be explained by the different electronic contributions from edges and the basal plane.[37] As the sheet size decreases, the contribution from edges sites relative to the basal plane increases changing the absorption coefficients. The extinction coefficients will also be affected, but note that the scattering will have an additional contribution on the extinction.

With the knowledge of the average nanosheet dimensions determined from AFM statistics, the size dependence of the extinction and absorbance spectra can be evaluated quantitatively. Figure 4C-D shows extinction (Figure 4C) and absorbance (Figure 4D) coefficients at selected wavelengths as a function of average nanosheet lateral size. At a wavelength of 900 nm, the extinction coefficient increases with <L> roughly as a power law, whereas in case of the absorbance coefficient it remains close to 0 across all sizes of <L>. This clear manifestation of the effect of scattering demonstrates that it is problematic to determine nanosheet concentrations using optical extinction coefficients alone. At most wavelengths in the resonant regime (e.g. 480 nm), both extinction and absorbance coefficients change with <L> due to edge effects. However, at specific wavelengths, the coefficients (both absorbance and extinction) are empirically found to be nearly size-invariant. For $Ni_2P_2S_6$, the size invariant wavelengths are 383 nm for extinction and 397 nm for absorbance, where we find the coefficients as $\varepsilon_{383nm} = 12.57 \pm 0.10\ L\mathrm{g}^{-1}\mathrm{cm}^{-1}$ and $\alpha_{397nm} = 8.14 \pm 0.06\ L\mathrm{g}^{-1}\mathrm{cm}^{-1}$.

This is useful, as it enables the reliable determination of the nanosheet concentration of unknown samples of any nanosheet size via the Beer Lambert law.

As a result of the variation in extinction/absorption coefficients with <L>, the intensity ratios in optical spectra scale with the nanosheet lateral sizes, which can be used to construct quantitative metrics for the size determination from optical spectra. For example, the ratio at 370 nm over 460nm versus the AFM mean lateral sheet size is plotted in Figure 4E. The data from both extinction and absorbance is included, showing a similar scaling. According to the model, assuming a different extinction/absorbance coefficient at the edge and centre of the basal planes, we expect the data to follow equation 1, with x as the thickness of the edge region and k being the nanosheet aspect ratio (length/width).[37]

$$\frac{Abs_{(\lambda 1)}}{Abs_{(\lambda 2)}} = \frac{\alpha_{(\lambda 1)}^{center} <L> + 2x(k+1)\Delta\alpha_{(\lambda 1)}}{\alpha_{(\lambda 2)}^{center} <L> + 2x(k+1)\Delta\alpha_{(\lambda 2)}} \qquad \text{Eq. 1}$$

While this is the case (see dashed line in Figure 4E), the relation is empirically almost linear for the intensity ratio in the accessible size range. Thus, to simplify calculations, we fit the data to a linear function (see solid line in Figure 4E) which gives the relationship between <L> and the peak intensity ratio as equation 2:

$$< L > \ (nm) = \frac{-480.8\ Ext_{370nm}}{Ext_{460nm}} - 815.7 \qquad \text{Eq. 2}$$

An alternative metric can be established using the scattering background in the non-resonant regime of the spectra. As recently demonstrated,[54] the scattering strength of platelet-like nanosheets is determined by the longest dimension, i.e. <L>. This results in the power law scaling of the extinction coefficient at 900 nm shown in Figure 4C. However, size determination from the extinction coefficient spectra requires the dispersion concentration to be determined independently, which greatly limits the feasibility of the approach. In contrast, peak intensities are always accessible and do not require knowledge of concentration. We find that a peak intensity ratio at a non-resonant to resonant wavelength also results in a power law scaling, as demonstrated by the plot of Ext_{900nm}/Ext_{460nm} in Figure 4F. Fitting gives equation 3 as an alternative metric for the determination of <L>:

$$< L > \ (nm) = 75.02\left(log\left(\frac{Ext_{900nm}}{Ext_{460nm}} + 0.03388\right) + 4.204\right) \qquad \text{Eq. 3}$$

As discussed above, understanding the optical spectra allows us to establish quantitative metrics for a reliable assessment of the dispersion concentration and <L>. While this is useful, it is of equal interest to determine the nanosheet layer number from the optical spectra. It was previously shown for transition metal dichalcogenides[26, 36, 37, 56] that layer number is reflected in changes of the energies of excitonic transitions due to confinement and dielectric screening effects. The absorbance spectra of $Ni_2P_2S_6$ show three broad features at 270, 370 and 460 nm (4.6, 3.4 and 2.7 eV). These were analysed with respect to changes in transition energy across

the samples. Since the peaks are broad and superimposed on a background, reliable determination of the peak position is only feasible via the second derivative. The second derivative of the extinction spectra in the region of 300-450 nm is shown for the first cascade in Figure 4G (for the 2nd cascade, see SI, Figure S10F). The well-developed negative signal in the second derivative can be used to read-off the centre of mass peak positions for both absorbance and extinction. A systematic red shift with increasing sheet thickness is observed. This behaviour agrees with literature data on excitonic transitions of TMDs[36, 37, 56] and GaS[26] which were also observed to red-shift with increasing thickness. The data is plotted as function of nanosheet layer number in Figure 4H. The thickness dependence of the peak positions within the size range studied here can be quantified by applying an appropriate empirical fit. This provides a metric to determine the nanosheet thickness from peak positions in both, absorption and extinction spectra as equation 4 and 5 respectively:

$$< N >_{Abs} = -4.383\ log\left(\frac{E(eV)-3.242}{0.1498}\right) + 1 \qquad \text{Eq. 4}$$

$$< N >_{Ext} = -5.797\ log\left(\frac{E(eV)-3.139}{0.3170}\right) + 1 \qquad \text{Eq. 5}$$

Note that the A-exciton peak positions of MoS_2[37] and WS_2[36] obtained from the second derivative are very similar from extinction and absorbance spectra, respectively. In contrast, for $Ni_2P_2S_6$, the peak position from the extinction spectra is significantly red-shifted compared to the absorbance data especially for larger/thicker nanosheets. We attribute this to a stronger contribution from light scattering in $Ni_2P_2S_6$ which is red-shifted to the absorbance in the resonant region (see SI, Figure S9).

In summary, a detailed understanding of the optical spectra is of great practical use, as it not only enables determination of the dispersion concentration, but also allows for a quantitative determination of the average nanosheet dimensions from readily available spectroscopic techniques. It is demonstrated that elimination of the scattering background is crucial to gain insights into these fundamental properties. For example, scattering completely masks the optical band edge in the extinction spectra but from the absorbance spectra, we find the optical gap shifts from 1.42 to 1.50 eV depending on the nanosheet dimensions.

Stability of $Ni_2P_2S_6$ nanosheets

This understanding of the optical absorbance/extinction for $Ni_2P_2S_6$ nanosheets can be exploited to study changes in the nanosheet properties over time. As mentioned above, XPS

measurements of the smaller/thinner nanosheets, i.e. those with higher surface area, showed some evidence of oxidation. It is thus crucial to investigate degradation in more detail.

To this end, the optical extinction and absorbance of fractions containing nanosheets with different lateral sizes and thicknesses were measured over time for different storage conditions. Samples were stored in the fridge (4°C) and stirred at 20, 40 and 60°C respectively. Prior to the measurement, samples were refreshed by bath sonication to avoid potential impact from sedimentation similar to previous work.[23, 24, 40, 57]

Extinction spectra from the small-sized sheets (3-10k *g*) stored at 20°C and 40°C for up to 488 hours are shown in figure 5A and 5B, respectively. Extinction and absorbance spectra of other sizes and storage conditions are shown in the SI (Figure S10, S12). Both extinction and absorbance (SI, Figure S11-13) spectra reveal a systematic decrease in intensity over time which we attribute to decomposition of the material. However, both spectral shapes remain largely consistent, confirming that the drop in intensity is not due to aggregation, as this would lead to an increased scattering background in the extinction. The decrease in optical density is more severe for storage at 40°C (Figure 5B) compared to 20°C (Figure 5A). Furthermore, a new peak at ~315 nm and a dip at ~290 nm are formed over time. In addition, an increase of the relative intensity at high energies is observed, which is a typical sign of oxidation, as nickel and phosphorous oxides tend to absorb in the UV region.[58-60] To track degradation-based changes systematically, the optical density at 460 nm is followed as a function of time, where the spectral shape remains unchanged in all cases.

The extinction intensity at 460 nm is plotted as function of time for the fraction containing small-sized (3-10k *g*) and large (0.6-3k *g*) nanosheets in figure 5C,D. Across all storage conditions, a roughly exponential decrease is observed. For both samples, the extinction approaches 0 for storage at 40°C or higher suggesting a complete decomposition of the material. For storage at 20, 40 and 60°C, we find the decay to be consistent with first order kinetics. This is illustrated by the plot of the natural logarithm of the optical density of the small-sized nanosheets as function of time in figure 5E. This clearly leads to a linearization of the data as expected for first order kinetics. Optical densities from extinction (filled symbols) and absorbance (open symbols) are included, confirming the agreement between both data sets. The fraction containing the largest nanosheets behaves the same way (see SI, Figure S13). Since fewer degrees of freedom are required to fit the linearized data in figure 5E than for the exponential fits in figure 5C and D, this allows the most reliable extraction of the macroscopic half-life for the degradation. The natural logarithm of the half-life is plotted as a function of inverse temperature in figure 5F for both medium and large nanosheets. Error bars represent the standard deviation of the fit. We find a linear scaling in this plot, allowing us to extract the activation energy of the degradation which is related to the slope according to the Arrhenius equation. We find activation energies of 20-30 meV with only minor differences for the two size fractions (small-sized: 23 meV, large-sized: 27 meV) supporting the hypothesis of the size-

independent degradation suggested above. This means that for $Ni_2P_2S_6$, oxidation occurs both at edges and on the basal planes. To the best of our knowledge, this is the first report where the activation energies for the degradation of nanosheets are assessed. Therefore, no comparison can be made to other layered materials that are known to be prone to oxidation such as BP,[24, 38, 61] TiS_2,[40] titanium carbides[57] or MoO_2[23].

Interestingly, the decay data of the samples stored in the refrigerator is distinct from the samples stored at room temperature or at elevated temperatures. This is demonstrated by the plot of the natural logarithm of the optical density at 460 nm as function of time in figure 5G. Clearly, the decay shows some non-linearity in particular at short storage times. While this appears puzzling at first glance, it is important to bear in mind that the vials were not sealed on storage. Hence, water from the environment condenses into the sample. We expect this effect to be more pronounced when the dispersions are stored in the refrigerator. If water was responsible for the degradation of the nanosheets, the degradation would be influenced by varying amounts of water over time. In such a case, one could anticipate a second order decay kinetic. To test this, we plot the inverse optical density as function of time in figure 5H. For both absorbance and extinction, a linear behaviour is observed which suggests that the decay follows a second order rate law; consistent with the hypothesis that nanosheet degradation occurs by reaction with water in the dispersion. Note that aggregation, which can be induced by the increased water content of the dispersion, would also result in a second order rate law. However, since we also do not observe an increased scattering background in the extinction spectra (see Figure S11A, S12A) for the sample sets stored in the fridge, we believe aggregation to play a minor role.

To further analyse the degradation behaviour, the local oxidation of single flakes was investigated by scanning TEM-EDX after stirring small-sized nanosheets (3-10k *g*) at 40°C for 500 hours. Elemental EDX maps (Ni, P, S, O) of a set of degraded nanosheets are displayed in figure 6A. In contrast to the freshly prepared sample (Figure S5), oxygen is not homogeneously distributed over the entire measurement frame, but shows contrast across the nanosheet due to surface oxidation. To analyse the degradation behaviour further, atomic percent maps were generated (insets in Figure 6A) by masking based on the Ni counts (Figure 6B, left) to reduce spurious signals from the support film. Applying other masks around the edge, the central region and an oxygen deficient region (highlighted by the white colour in Figure 6B) allows us to extract the local stoichiometry of different parts of the flake. The nanosheet edges show a relatively high concentration of P with a stoichiometry of $Ni_{0.8}P_1S_1$, while the central mask yields $Ni_{0.8}P_1S_{1.8}$. In the oxygen-depleted region towards the centre of the larger nanosheet, the local stoichiometry is $Ni_{0.9}P_1S_{2.7}$, *i.e.* much closer to the expected composition measured for the freshly prepared nanosheet ($NiPS_{2.8}$, Figure S5). This deviation of the composition from that found for the freshly prepared nanosheet illustrates that in particular sulfur is dissolved and removed during oxidative degradation. While the change in the stoichiometry is more

pronounced at the edge compared to the basal plane, it is important to bear in mind that the edge is fully exposed to the environment, while inner layers of a few-layered sheet are protected. Hence overall the STEM-EDX analysis confirms that degradation occurs both on edge and basal plane.

Conclusions

In summary, $Ni_2P_2S_6$ crystals were liquid-exfoliated in CHP. Going beyond published work on LPE of this material,[10] we performed size selection by cascade centrifugation and quantified the size and thickness distributions by AFM statistics. Nanosheets dispersions with an average layer number of 4 could be obtained in the fraction isolated at high centrifugal accelerations, while the mean layer number was 16 when low centrifugal accelerations were used. The robustness of liquid cascade centrifugation is proven by evaluation of two batches size selected with different centrifugation steps. Knowledge of size and thickness distribution enabled the development of quantitative spectroscopic metrics for concentration, length and thickness by correlating AFM statistics to optical extinction and absorbance spectroscopy.

Further structural characterisation showed that the exfoliated nanosheets remain widely intact and crystalline after exfoliation and size selection. XPS revealed some oxidation that scaled with the accessible surface area/volume. To gain a deeper understanding of the degradation behaviour, the stability of the nanosheets was investigated by temperature and time dependent extinction/absorbance spectroscopy. At 20°C, approximately 80% of exfoliated material remains intact after 100 h which is a sufficient timeframe for further processing. The kinetics of the degradation follow a 1st order rate law. Arrhenius plots of the temperature dependent data allowed us to determine activation energies for degradation, which are in the range of 20-30 kJ/mol. Only a marginal size dependence for the decomposition was observed which supports the conclusion from XPS that oxidation occurs on both edge sites and on the basal plane. This is further confirmed by STEM/EDX.

This work provides an important guide for researchers interested in exploiting the electrochemical, magnetic or optical properties of $Ni_2P_2S_6$ nanosheets. The metrics described here can be used to precisely determine concentration and nanosheet dimensions which will be of great practical use for future work on studying size/thickness dependent properties in energy application. Furthermore, knowledge of the size/thickness dependent absorbance can be helpful to explore $Ni_2P_2S_6$ in photoelectrocatalysis or optoelectronic applications (e.g. photodetectors, where CVD grown $Ni_2P_2S_6$ showed promise[62]). In addition, the quantification of the degradation kinetics provides the available timeframe for further processing. The observed degradation in the presence of water and oxygen also implies that care has to be taken when studying the electrocatalytic water splitting performance of $Ni_2P_2S_6$ nanosheets and related structures. Further work will be required to decouple catalytic effects from intact nanosheets

and their degradation products. To this end, our relatively simple strategy to determine activation energies for nanosheet degradation is a powerful approach, as it can be readily applied to other nanomaterial dispersions and will enable quantitative comparison of the stability of systems with different chemical composition, structure, doping or solvent environment.

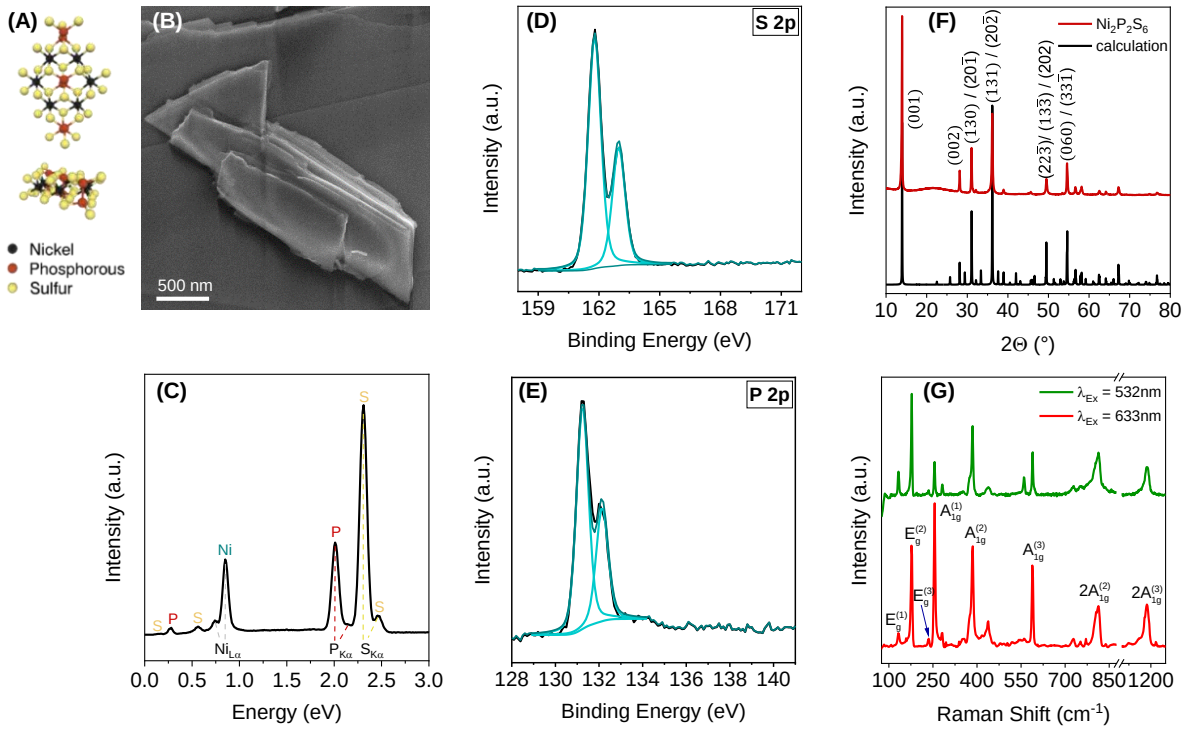

Figure 1. **Characterisation of the bulk material**. (A) Schematic view of the $Ni_2P_2S_6$ crystal structure. (B) SEM image of a bulk crystal shows the layered structure of the material (SEI, 5 kV, WD = 3 mm). (C) EDX measurements show only the expected signals from Ni, P and S. (D), (E) Fitted XPS S_{2p} and P_{2p} core level spectra, respectively, showing a single doublet in each case. (F) Simulated [41] (space group *C2/m*) and measured X-ray diffractogram. (G) Raman spectra normalised to the E_{2g} vibrational mode at 177 cm^{-1} for excitation with a 532 and 633 nm laser.

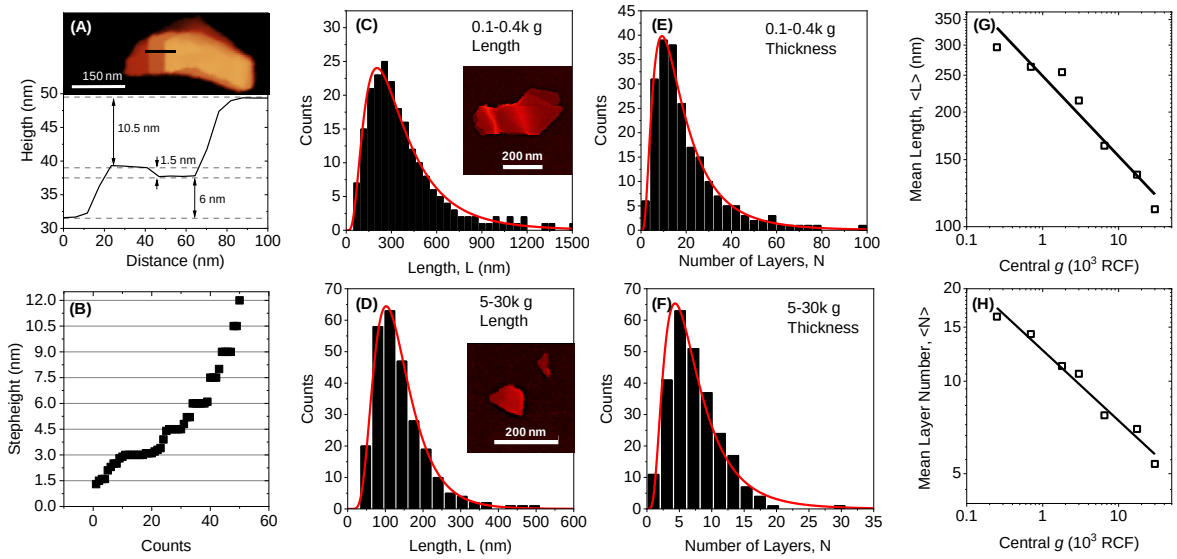

Figure 2. **AFM statistics on size-selected fractions**. (A) Height profile of the nanosheet along the black line. Steps of multiple layers are clearly resolved. (B) Height of terraces of incompletely exfoliated nanosheets (step height) in ascending order. The step height is found to be a multiple of 1.5 nm which is the apparent AFM height of one layer and used to covert the measured AFM height to layer number. (C-D) histograms of lateral sheet size distribution of drop-cast nanosheets for two fractions containing relatively large nanosheets, RCF = 0.1-0.4k g (C) and small sheets, RCF = 5-30k g (D). The insets show representative nanosheets of the respective fraction. (E-F) histograms of layer number, N, for the same fractions as in (C-D). G) Plot of mean nanosheet length, <L>, as function of the midpoint of the pair of centrifugal accelerations used in LCC. H) Plot of arithmetic mean nanosheet layer number, <N>, as function of the midpoint of the pair of centrifugal accelerations used in LCC. The data in (G) and (H) is characterised by a power law scaling as indicated by the solid line.

Table 1. **Overview of nanosheet dimensions** displaying the mean nanosheet length, <L>, arithmetic mean layer number, <N> and gravimetric yield of all fractions of the $Ni_2P_2S_6$ dispersions obtained in the two centrifugation cascades. For each data set the top row gives the RCF range used in the centrifugation. In both cases, the first fraction (large unexfoliated material) was not subjected to further characterisation.

Sizes	0-0.1k *g*	0.1-0.4k *g*	0.4-1k *g*	1-5k *g*	5-30k *g*
<L> (nm)	-	296	263	215	137
<N> (Layers)	-	16.2	14.2	10.5	7.0
Yield (%)	67.1	11.3	9.0	5.0	3.9

Sizes	0-0.6k *g*	0.6-3k *g*	3-10k *g*	10-50k *g*
<L> (nm)	-	255	163	111
<N> (Layers)	-	11.2	7.7	5.4
Yield (%)	80.5	6.7	5.6	3.6

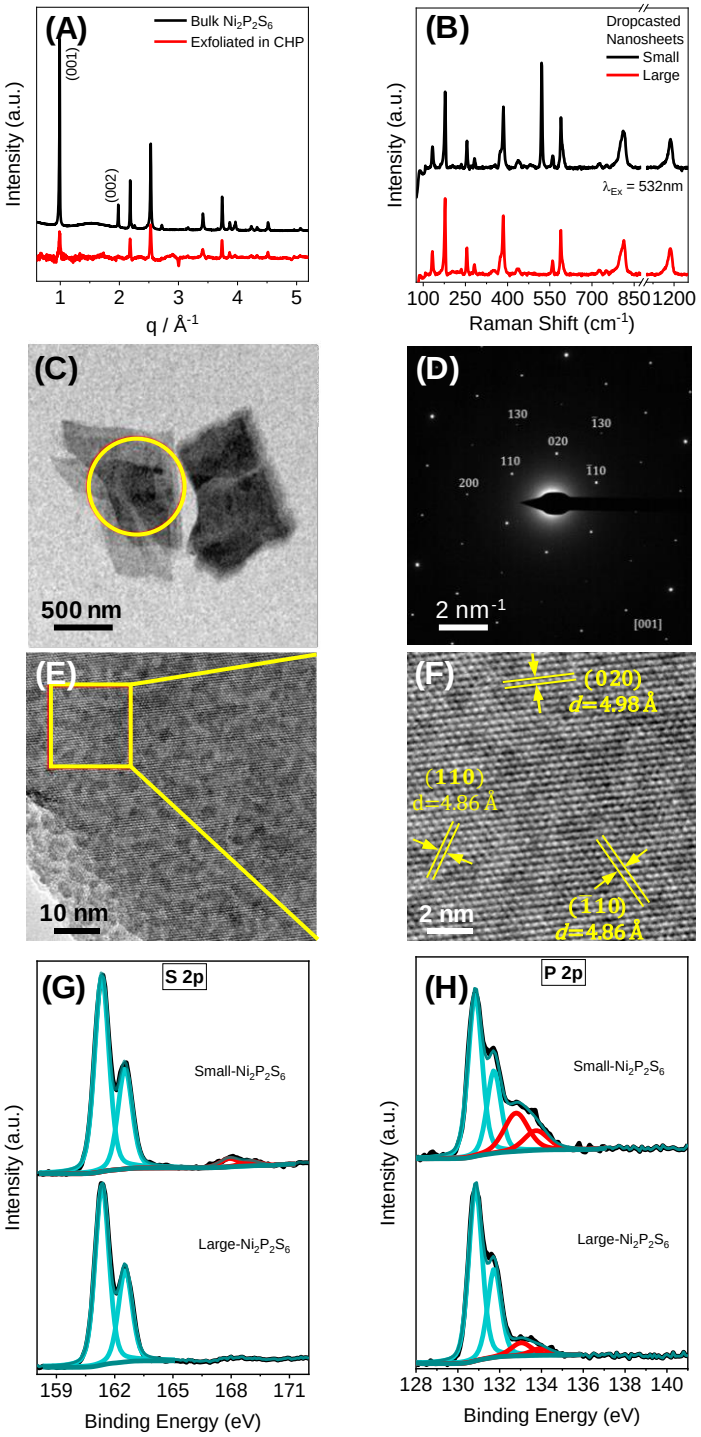

Figure 3. **Characterisation of the nanosheets.** (A) XRD measurements the bulk crystal (black) compared to exfoliated nanosheets in dispersion (CHP, red). As the XRD pattern of the exfoliated sample was collected at DESY, P02.1 and the pattern of the bulk sample in-house, both patterns are plotted in q-space for a better comparability. The background of the dispersion medium CHP was subtracted from the diffractogram of the exfoliated sample using a simple spline fit method. (B) Raman measurements on drop-cast samples of small (5-30k *g*) and large (0.1-0.4k *g*) nanosheets. Residual CHP was removed in vacuum at 60°C overnight. (C) Bright

field TEM image of the large nanosheets. The yellow circle indicates the probed area for the electron diffraction measurement. (D) shows the SAED pattern of the nanosheet in (C). (E), (F) HRTEM image of $Ni_2P_2S_6$ nanosheets viewed along [001]. The lattice spacings indicated by the yellow bars are 4.98 Å, 4.86 Å and 4.86 Å corresponding to the (020), (110) and ($\bar{1}$10) crystal planes respectively. (G) and (F) show XPS S_{2p} and P_{2p} core level spectra of drop-cast nanosheets.

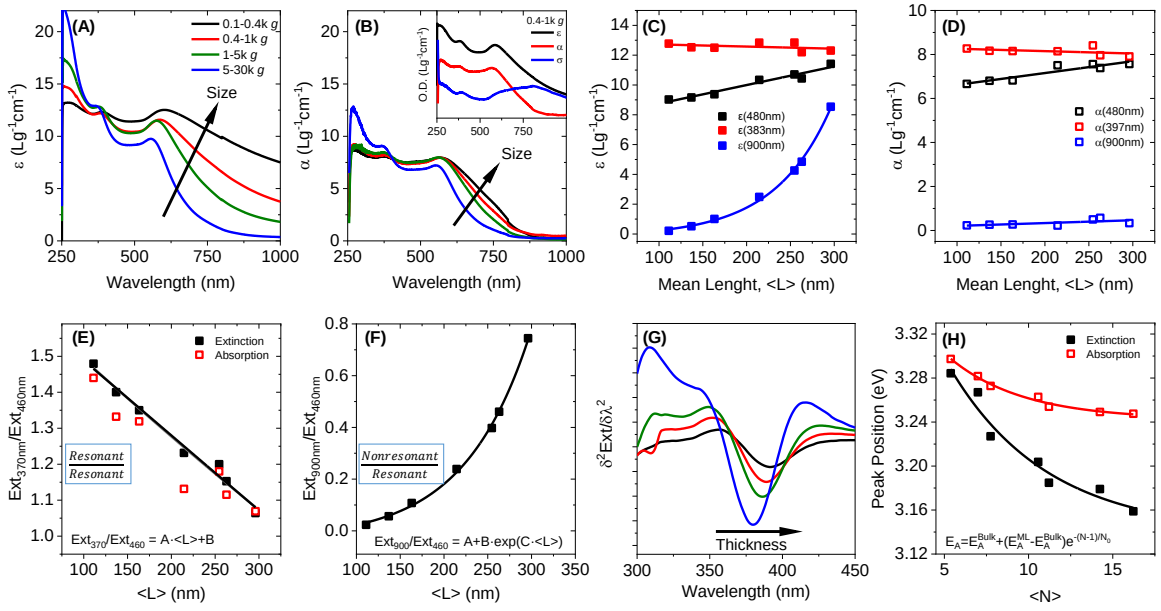

Figure 4. **Metrics derived from optical spectroscopy.** (A) and (B) show the size-dependent extinction (A) and absorption (B) coefficients as function of wavelength. Extinction coefficients, ε, for different sizes merge at 383 nm (397 nm for absorption, α). The inset shows a direct comparison of extinction, absorbance and scattering for fraction 0.4-1k *g*. (C, D) Plots of extinction (C) and absorbance (D) coefficient at selected wavelengths as a function of <L>. The increase of α and ε at 480 nm is due to a change in the edge site to basal plane ratio. Exponential increase of ε at 900 nm is due to scattering effects. (E) Peak intensity ratio at 370 nm/460 nm plotted versus mean lateral size of the nanosheets. The data can be approximated by a linear fit (solid line). (F) Peak intensity ratio at 900 nm/460 nm plotted versus mean lateral size of the nanosheets. Power law scaling due to the huge scattering contribution at 900 nm is observed. (G) Second derivative of the extinction allows determination of the center of mass peak positions. Peaks redshift with increasing nanosheet dimensions. (H) Plot of center of mass peak positions as function of mean layer number extracted from extinction and absorbance spectra.

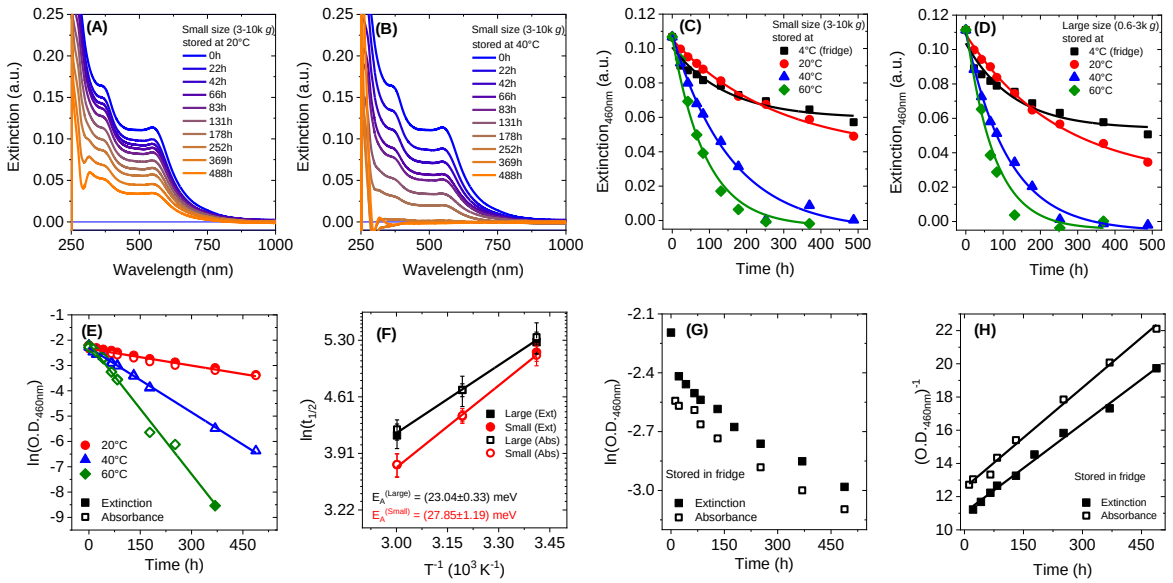

Figure 5. **Degradation of the $Ni_2P_2S_6$ nanosheets.** (A) and (B) extinction spectra of medium sized $Ni_2P_2S_6$ nanosheets in dispersion, stirred at 20°C (A) and 40°C (B) respectively measured at different times after preparation. (C) and (D) show the exponential decay of the extinction plateau at 460 nm for small (C) and large (D) fractions. (E) Extinction and absorption at 460 nm of the fraction containing small nanosheets stored at 20, 40 and 60°C, respectively as function of time (plotted on a semi-ln scale). Data from both absorbance and extinction is included and falls on the same curve. Solid lines are linear fits to extract the degradation half-lives. (F) Plot of the half-lives as a function of inverse temperature on a semi-ln scale. Lines are linear fits to extract the average activation energy of the degradation process. (G) Plot of extinction and absorption at 460 nm (small nanosheets) as function of time plotted on a semi-ln scale for the sample stored in the refrigerator. No linearization of the data is observed. (H) Same data as in (G) plotted as inverse optical density at 460 nm as function of time. Linear fits suggest second order kinetics.

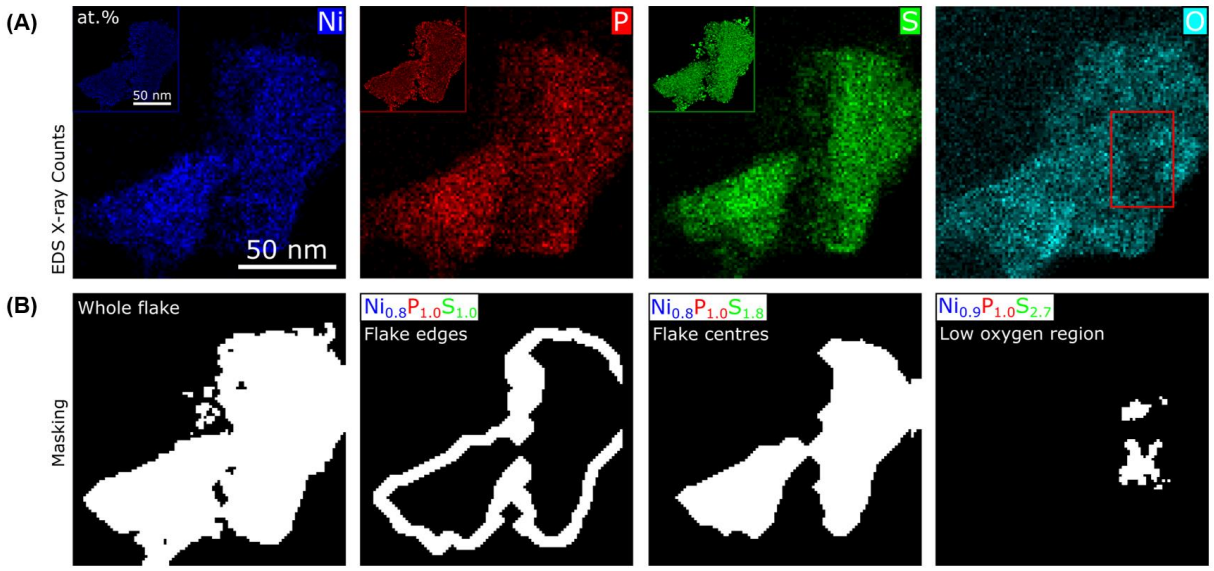

Figure 6. **Measurement of local oxidation using STEM-EDX.** (A) EDX maps of two flakes showing oxygen distributed within and on the surface as well as on the surrounding carbon support. Atomic percent maps showing the Ni:P:S ratio (inset) show a relatively high concentration of P at the flake edges. Absolute quantification fo the O signal is not possible due to the presence of oxygen in the carbon support. (B) Quantification of the the Ni:P:S ratio in different regions of the flake was achieved by masking the raw spectrum image using the masks shown (where the signal from the white areas is included and black areas are excluded). The location of the flakes was determined based on the presence of Ni counts. The 'flake edges' mask yields a $Ni_xP_yS_z$ ratio of 0.8:1:1 (x:y:z) and the 'flake centres' mask yields 0.8:1.0:1.8. A relatively pristine ('low oxygen region') towards the centre of the larger flake (region highlighted by the red rectangle on the O map) gives a ratio of 0.9:1.0:2.7.

Experimental Methods:

Material synthesis

$Ni_2P_2S_6$ was synthesised via high temperature solid state reaction as reported by Rao et al.[41] Stoichiometric amounts of elemental nickel, red phosphorous and sulfur were heated in evacuated quartz tubes (10^{-4} mbar) within 4 h to 450°C. The temperature is kept for one day and then further heated to 650°C within 2 h for one week.

Liquid-phase exfoliation

50 mg of ground $Ni_2P_2S_6$ crystals were sonicated over 5 h in 25 ml of solvent using a sonic tip (Vibracell VCX, 750 W, tapered tip, order number 630-0418) at 40 % amplitude in a 4 s on, 4 s off, pulse sequence. The dispersion was kept in a 4°C cooling cell during sonication in order to avoid heating effects. Samples prepared according to this protocol are referred to as stock dispersion.

Size selection

Dispersions were size-selected by liquid cascade centrifugation in multiple steps of subsequently increasing centrifugation speeds. For centrifugation speeds up to 30k *g*, a Hettich Mikro 220R centrifuge equipped with a fixed-angle rotor (1195A) was used. For centrifugation at 50k *g*, a Beckman Coulter Avanti XP centrifuge was used with a fixed angle rotor (JA25.15). Each centrifugation step was performed for 2 hours at 20°C. Two sets of samples were prepared to obtain different distributions of nanosheet sizes. The first set of samples was prepared using a centrifugal acceleration of 0.1, 0.4, 1, 5, and 30k *g*. The speeds for the second set were 0.6, 3, 10 and 50k *g*. After each step, the sediment was redispersed for analysis in a reduced solvent volume (~ 1 mL CHP) and the supernatant was used for the subsequent step. The expression "0.1-0.4k *g*" describes consecutive centrifugation steps. In this example, the sample was obtained by sedimentation of nanosheets at 400 g from the supernatant obtained after centrifugation at 100 *g*. The central *g*-force used in figure 4 is given by the mean centrifugal acceleration between two steps (in this example: 0.25k *g*).

Gravimetry:

The concentration of nanomaterial in each fraction was determined by filtering a known volume of dispersion onto AlOx membranes (pore size 20 nm) and washing with 1 L Isopropanol. Prior to weighing, membranes were dried overnight in vacuum at 60°C.

Extinction and absorbance

Optical extinction and absorbance measurements were carried out with an Agilent Cary 6000i spectrometer in quartz cuvettes. The spectrometer was equipped with an integrating sphere (external DRA-1800) for absorbance measurements. In this case, the cuvettes were placed in the center of the sphere. The optical density of the dispersions was adjusted to 0.3−0.4 at the peak. The measurements of both, extinction and absorbance spectra allow for the calculation of scattering spectra (Ext−Abs). All spectra were acquired with 0.5 nm increments and 0.1 s integration time.

Raman

Raman spectroscopy was carried out on a Renishaw InVia-Reflex confocal Raman microscope with a 532 nm excitation laser in air under ambient conditions. The Raman emission was collected by a 50× long working distance objective lens in streamline mode and dispersed by a 2400 l/mm grating with 1% of the laser power (<10 μW). The spectrometer was calibrated to a silicon reference sample prior to the measurement to correct for the instrument response. Liquid dispersions were dropped (~20μL) onto Si/SiO_2 wafers and left to dry in vacuum at 60°C overnight before measuring. For each sample, 50 spectra were accumulated on 3 different positions and averaged. In the streamline mode, where a larger sample area is probed, no spot to spot variations were observed except for absolute intensities.

SEM/EDX

SEM images were acquired with a JEOL JSM-7610F field emission scanning electron microscope (FE-SEM), using an In-lens Schottky field emission electron gun with 5 kV acceleration voltage at $2.5x10^{-9}$ mbar. The images were measured with a dual (upper and lower) detector system consisting of collector-, scintillator-, light guide- and photomultiplier units for secondary electron imaging (SEI). EDX was performed at 15 kV, at 9 mm working distance, using a Thermo-Scientific 30mm²-UltraDry silicon drift detector for x-ray detection in 28.5° angle to the specimen.

AFM

Atomic force microscopy (AFM) was carried out on a Dimension ICON3 scanning probe microscope (Bruker AXS S.A.S.) in ScanAsyst in air under ambient conditions using aluminium coated silicon cantilevers (OLTESPA-R3). The concentrated dispersions were diluted with isopropanol to optical densities <0.1 at 500 nm. A drop of the dilute dispersions (15 μL) was deposited on pre-heated (180°C) Si/SiO_2 wafers (0.5x0.5 cm^2) with an oxide layer of 300 nm. After deposition, the wafers were rinsed with ~5 mL of water and ~5 mL of isopropanol and dried with compressed nitrogen. Typical image sizes ranged from 20x20 for larger nanosheets to 5x5 μm^2 at scan rates of 0.5-0.8 Hz with 1024 lines per image. Step height analysis was used to convert the apparent AFM thickness to layer number as discussed in the

main manuscript. Previously published length corrections were used to correct lateral dimensions from cantilever broadening.[49]

TEM sample preparation and characterisation

The samples for (S)TEM measurements were sonicated in a sonication bath for about 2 hours at room temperature in order to split the agglomerated nanosheets. After sonication, the $Ni_2P_2S_6$ colloids were drop-cast onto carbon-coated copper TEM grids and dried at 100 ˚C for 2 hours in a vacuum system (~$2.7x10^{-5}$ mbar). TEM imaging and diffraction measurements were performed in an FEI Tecnai G2 20 TEM at 200 kV at room temperature.

High angle annular dark field (HAADF)-STEM imaging was performed in an FEI Titan G2 80-200 'ChemiSTEM' operated at 200 kV. STEM-EDX data was acquired with the Titan's Super-X detector system, with all four detectors used for a total collection angle of ~0.7 srad. All STEM-EDX data was processed in Hyperspy and quantification was performed using the Cliff-Lorimer method with standardless k-factors.

XRD

XRD patterns of the bulk material were collected in Debye-Scherrer geometry using Cu $K_{\alpha 1}$ radiation (λ = 1.54058 Å) with a PANalytical Empyrean diffractometer equipped with a PIXcel1D detector. XRD patterns of the exfoliated dispersion of $Ni_2P_2S_6$ were collected at beamline P02.1, Petra III, DESY, Hamburg at a wavelength λ = 0.207 Å (60 keV) and a sample detector distance of 1010 mm. The detector used was a PerkinElmer XRD1621 two-dimensional (2D) detector. The 2D data was processed using the software DAWN Science.[63] To account instrumental contributions to XRD, a NIST 660a LaB_6 reference material was measured.

XPS

For XPS, the bulk material was glued on Capton tape, the size-selected dispersions were filtered on alumina membranes. The stock was drop-cast on ITO to also capture the signal from very small nanosheets and potential oxidation products. XPS measurements were carried out with an ESCALAB 250Xi (Thermo Scientific) in ultrahigh vacuum, an XR6 monochromated Al Kα source ($h\nu$ = 1486.6 eV), and a pass energy of 20 eV. XPS of samples prepared on non-conducting substrates was measured with charge compensation employing a flood electron source.

Acknowledgements

C.B. acknowledges support from the German research foundation (DFG) under grant agreement Emmy-Noether, BA4856/2-1 and Jana Zaumseil for the access to the infrastructure at the Chair of Applied Physical Chemistry. W.B. acknowledges DESY (Hamburg, Germany), a member of the Helmholtz Association HGF, for the provision of experimental facilities. Parts of this research were carried out at PETRA III and we would like to thank Martin Etter for assistance in using beamline P02.1. S.J.H, S.S and D.J.K thank the U.K. Engineering and Physical Sciences Research Council (EPSRC) (EP/P009050/1) and the European Research Council (ERC) under the European Union's Horizon 2020 research and innovation program (Grant Agreement ERC-2016-STG-EvoluTEM-715502).

Supporting information

Atomic force microscopy statistics, Raman spectroscopy, TEM, XPS, optical extinction and absorbance, degradation kinetics of nanosheets

Competing financial interests

The authors declare no competing financial interests.

References

1. Académie des sciences, C. n. d. l. r. s., *Comptes rendus hebdomadaires des séances de l'Académie des sciences*. publiés avec le concours du Centre national de la recherche scientifique par MM: Paris, 1894; Vol. 118 (1), p. 260-264.
2. Taylor, B. E.; Steger, J.; Wold, A., Preparation and properties of some transition metal phosphorus trisulfide compounds. *J. Solid State Chem.* **1973,** 7, 461-467.
3. Susner, M. A.; Chyasnavichyus, M.; McGuire, M. A.; Ganesh, P.; Maksymovych, P., Metal Thio- and Selenophosphates as Multifunctional van der Waals Layered Materials. *Adv. Mater.* **2017,** 29, 1602852.
4. Gusmão, R.; Sofer, Z.; Pumera, M., Metal Phosphorous Trichalcogenides (MPCh3): From Synthesis to Contemporary Energy Challenges. *Angew. Chem. Int. Ed.* **2019,** 58, 9326-9337.
5. Mayorga-Martinez, C. C.; Sofer, Z.; Sedmidubský, D.; Huber, Š.; Eng, A. Y. S.; Pumera, M., Layered Metal Thiophosphite Materials: Magnetic, Electrochemical, and Electronic Properties. *ACS Appl. Mater. Interfaces* **2017,** 9, 12563-12573.
6. Barj, M.; Sourisseau, C.; Ouvrard, G.; Brec, R., Infrared studies of lithium intercalation in the FePS3 and NiPS3 layer-type compounds. *Solid State Ionics* **1983,** 11, 179-183.
7. Whittingham, M. S., Intercalation chemistry and energy storage. *J. Solid State Chem.* **1979,** 29, 303-310.
8. Harvey, A.; Backes, C.; Gholamvand, Z.; Hanlon, D.; McAteer, D.; Nerl, H. C.; McGuire, E.; Seral-Ascaso, A.; Ramasse, Q. M.; McEvoy, N.; Winters, S.; Berner, N. C.; McCloskey, D.; Donegan, J. F.; Duesberg, G. S.; Nicolosi, V.; Coleman, J. N., Preparation of Gallium Sulfide Nanosheets by Liquid Exfoliation and Their Application As Hydrogen Evolution Catalysts. *Chem. Mater.* **2015,** 27, 3483-3493.

9. Liu, X.; Zeng, J.; Yang, H.; Zhou, K.; Pan, D., V2O5-Based nanomaterials: synthesis and their applications. *RSC Adv.* **2018,** 8, 4014-4031.
10. Dangol, R.; Dai, Z.; Chaturvedi, A.; Zheng, Y.; Zhang, Y.; Dinh, K. N.; Li, B.; Zong, Y.; Yan, Q., Few-layer NiPS3 nanosheets as bifunctional materials for Li-ion storage and oxygen evolution reaction. *Nanoscale* **2018,** 10, 4890-4896.
11. Jenjeti, R. N.; Austeria, M. P.; Sampath, S., Alternate to Molybdenum Disulfide: A 2D, Few-Layer Transition-Metal Thiophosphate and Its Hydrogen Evolution Reaction Activity over a Wide pH Range. *ChemElectroChem* **2016,** 3, 1392-1399.
12. Cai, Z.; Liu, B.; Zou, X.; Cheng, H.-M., Chemical Vapor Deposition Growth and Applications of Two-Dimensional Materials and Their Heterostructures. *Chem. Rev.* .**2018,** 118, 6091-6133.
13. Yi, M.; Shen, Z., A review on mechanical exfoliation for the scalable production of graphene. *J. Mater. Chem. C.* **2015,** 3, 11700-11715.
14. Tao, H.; Zhang, Y.; Gao, Y.; Sun, Z.; Yan, C.; Texter, J., Scalable exfoliation and dispersion of two-dimensional materials - an update. *Phys. Chem. Chem. Phys.* **2017,** 19, 921-960.
15. Hu, G.; Kang, J.; Ng, L. W. T.; Zhu, X.; Howe, R. C. T.; Jones, C. G.; Hersam, M. C.; Hasan, T., Functional inks and printing of two-dimensional materials. *Chem. Soc. Rev.* **2018,** 47, 3265-3300.
16. Lotya, M.; Hernandez, Y.; King, P. J.; Smith, R. J.; Nicolosi, V.; Karlsson, L. S.; Blighe, F. M.; De, S.; Wang, Z.; McGovern, I. T.; Duesberg, G. S.; Coleman, J. N., Liquid Phase Production of Graphene by Exfoliation of Graphite in Surfactant/Water Solutions. *J. Am. Chem. Soc.* **2009,** 131, 3611-3620.
17. Hernandez, Y.; Nicolosi, V.; Lotya, M.; Blighe, F. M.; Sun, Z.; De, S.; McGovern, I. T.; Holland, B.; Byrne, M.; Gun'Ko, Y. K.; Boland, J. J.; Niraj, P.; Duesberg, G.; Krishnamurthy, S.; Goodhue, R.; Hutchison, J.; Scardaci, V.; Ferrari, A. C.; Coleman, J. N., High-yield production of graphene by liquid-phase exfoliation of graphite. *Nat. Nanotechnol.* **2008,** 3, 563-568.
18. Zhi, C.; Bando, Y.; Tang, C.; Kuwahara, H.; Golberg, D., Large-Scale Fabrication of Boron Nitride Nanosheets and Their Utilization in Polymeric Composites with Improved Thermal and Mechanical Properties. *Adv. Mater.* **2009,** 21, 2889-2893.
19. Griffin, A.; Harvey, A.; Cunningham, B.; Scullion, D.; Tian, T.; Shih, C.-J.; Gruening, M.; Donegan, J. F.; Santos, E. J. G.; Backes, C.; Coleman, J. N., Spectroscopic Size and Thickness Metrics for Liquid-Exfoliated h-BN. *Chem. Mater.* **2018,** 30, 1998-2005.
20. Coleman, J. N.; Lotya, M.; O'Neill, A.; Bergin, S. D.; King, P. J.; Khan, U.; Young, K.; Gaucher, A.; De, S.; Smith, R. J.; Shvets, I. V.; Arora, S. K.; Stanton, G.; Kim, H.-Y.; Lee, K.; Kim, G. T.; Duesberg, G. S.; Hallam, T.; Boland, J. J.; Wang, J. J.; Donegan, J. F.; Grunlan, J. C.; Moriarty, G.; Shmeliov, A.; Nicholls, R. J.; Perkins, J. M.; Grieveson, E. M.; Theuwissen, K.; McComb, D. W.; Nellist, P. D.; Nicolosi, V., Two-Dimensional Nanosheets Produced by Liquid Exfoliation of Layered Materials. *Science* **2011,** 331, 568-571.
21. Smith, R. J.; King, P. J.; Lotya, M.; Wirtz, C.; Khan, U.; De, S.; O'Neill, A.; Duesberg, G. S.; Grunlan, J. C.; Moriarty, G.; Chen, J.; Wang, J.; Minett, A. I.; Nicolosi, V.; Coleman, J. N., Large-Scale Exfoliation of Inorganic Layered Compounds in Aqueous Surfactant Solutions. *Adv. Mater.* **2011,** 23, 3944-3948.
22. Hanlon, D.; Backes, C.; Higgins, T. M.; Hughes, M.; O'Neill, A.; King, P.; McEvoy, N.; Duesberg, G. S.; Mendoza Sanchez, B.; Pettersson, H.; Nicolosi, V.; Coleman, J. N., Production of Molybdenum Trioxide Nanosheets by Liquid Exfoliation and Their Application in High-Performance Supercapacitors. *Chem. Mater.* **2014,** 26, 1751-1763.
23. Boland, J. B.; Harvey, A.; Tian, R.; Hanlon, D.; Vega-Mayoral, V.; Szydłowska, B. M.; Griffin, A.; Stimpel-Lindner, T.; Metel, S.; Nicolosi, V.; Duesberg, G.; Coleman, J. N., Liquid phase exfoliation of MoO2 nanosheets for lithium ion battery applications. *Nanoscale Adv.* **2019**.
24. Hanlon, D.; Backes, C.; Doherty, E.; Cucinotta, C. S.; Berner, N. C.; Boland, C.; Lee, K.; Lynch, P.; Gholamvand, Z.; Harvey, A.; Zhang, S.; Wang, K.; Moynihan, G.; Pokle, A.; Ramasse, Q. M.; McEvoy, N.; Blau, W. J.; Wang, J.; Abellan, G.; Hauke, F.; Hirsch, A.; Sanvito, S.; O'Regan, D. D.; Duesberg, G. S.; Nicolosi, V.; Coleman, J. N., Liquid Exfoliation of Solvent-Stabilised Few-Layer Black Phosphorus for Applications Beyond Electronics. *Nature Commun.* **2015,** 6, 8563.
25. Kang, J.; Wood, J. D.; Wells, S. A.; Lee, J.-H.; Liu, X.; Chen, K.-S.; Hersam, M. C., Solvent Exfoliation of Electronic-Grade, Two-Dimensional Black Phosphorus. *ACS Nano* **2015,** 9, 3596-3604.

26. Harvey, A.; Backes, C.; Gholamvand, Z.; Hanlon, D.; McAteer, D.; Nerl, H. C.; McGuire, E.; Seral-Ascaso, A.; Ramasse, Q. M.; McEvoy, N.; Winters, S.; Berner, N. C.; McCloskey, D.; Donegan, J.; Duesberg, G.; Nicolosi, V.; Coleman, J. N., Preparation of Gallium Sulfide Nanosheets by Liquid Exfoliation and Their Application As Hydrogen Evolution Catalysts. *Chem. Mater.* **2015,** 27, 3483–3493.
27. Petroni, E.; Lago, E.; Bellani, S.; Boukhvalov, D. W.; Politano, A.; Gürbulak, B.; Duman, S.; Prato, M.; Gentiluomo, S.; Oropesa-Nuñez, R.; Panda, J.-K.; Toth, P. S.; Del Rio Castillo, A. E.; Pellegrini, V.; Bonaccorso, F., Liquid-Phase Exfoliated Indium–Selenide Flakes and Their Application in Hydrogen Evolution Reaction. *Small* **2018,** 14, 1800749.
28. Brent, J. R.; Lewis, D. J.; Lorenz, T.; Lewis, E. A.; Savjani, N.; Haigh, S. J.; Seifert, G.; Derby, B.; O'Brien, P., Tin(II) Sulfide (SnS) Nanosheets by Liquid-Phase Exfoliation of Herzenbergite: IV–VI Main Group Two-Dimensional Atomic Crystals. *J. Am. Chem. Soc.* **2015,** 137, 12689-12696.
29. Zhang, P.; Zhao, F.; Long, P.; Wang, Y.; Yue, Y.; Liu, X.; Feng, Y.; Li, R.; Hu, W.; Li, Y.; Feng, W., Sonication-assisted liquid-phase exfoliated α-GeTe: a two-dimensional material with high Fe3+ sensitivity. *Nanoscale* **2018,** 10, 15989-15997.
30. Harvey, A.; He, X.; Godwin, I. J.; Backes, C.; McAteer, D.; Berner, N. C.; McEvoy, N.; Ferguson, A.; Shmeliov, A.; Lyons, M. E. G.; Nicolosi, V.; Duesberg, G. S.; Donegan, J. F.; Coleman, J. N., Production of Ni(OH)2 nanosheets by liquid phase exfoliation: from optical properties to electrochemical applications. *J. Mater. Chem. C.* **2016,** 4, 11046-11059.
31. McAteer, D.; Godwin, I. J.; Ling, Z.; Harvey, A.; He, L.; Boland, C. S.; Vega-Mayoral, V.; Szydłowska, B.; Rovetta, A. A.; Backes, C.; Boland, J. B.; Chen, X.; Lyons, M. E. G.; Coleman, J. N., Liquid Exfoliated Co(OH)2 Nanosheets as Low-Cost, Yet High-Performance, Catalysts for the Oxygen Evolution Reaction. *Adv. En. Mater.* **2018,** 0, 1702965.
32. Harvey, A.; Boland, J. B.; Godwin, I.; Kelly, A. G.; Szydłowska, B. M.; Murtaza, G.; Thomas, A.; Lewis, D. J.; O'Brien, P.; Coleman, J. N., Exploring the versatility of liquid phase exfoliation: producing 2D nanosheets from talcum powder, cat litter and beach sand. *2D Mater.* **2017,** 4, 025054.
33. Hughes, J. M.; Aherne, D.; Coleman, J. N., Generalizing solubility parameter theory to apply to one- and two-dimensional solutes and to incorporate dipolar interactions. *J. Appl. Polym. Sci.* **2013,** 127, 4483-4491.
34. Smith, R. J.; Lotya, M.; Coleman, J. N., The importance of repulsive potential barriers for the dispersion of graphene using surfactants. *New J. Phys.* **2010,** 12, 125008.
35. Kang, J.; Sangwan, V. K.; Wood, J. D.; Hersam, M. C., Solution-Based Processing of Monodisperse Two-Dimensional Nanomaterials. *Acc. Chem. Res.* **2017,** 50, 943-951.
36. Backes, C.; Szydłowska, B. M.; Harvey, A.; Yuan, S.; Vega-Mayoral, V.; Davies, B. R.; Zhao, P.-l.; Hanlon, D.; Santos, E. J. G.; Katsnelson, M. I.; Blau, W. J.; Gadermaier, C.; Coleman, J. N., Production of Highly Monolayer Enriched Dispersions of Liquid-Exfoliated Nanosheets by Liquid Cascade Centrifugation. *ACS Nano* **2016,** 10 1589-1601.
37. Backes, C.; Smith, R. J.; McEvoy, N.; Berner, N. C.; McCloskey, D.; Nerl, H. C.; O'Neill, A.; King, P. J.; Higgins, T.; Hanlon, D.; Scheuschner, N.; Maultzsch, J.; Houben, L.; Duesberg, G. S.; Donegan, J. F.; Nicolosi, V.; Coleman, J. N., Edge and Confinement Effects Allow in situ Measurement of Size and Thickness of Liquid-Exfoliated Nanosheets. *Nature Commun.* **2014,** 5, 4576.
38. Castellanos-Gomez, A.; Vicarelli, L.; Prada, E.; Island, J. O.; Narasimha-Acharya, K. L.; Blanter, S. I.; Groenendijk, D. J.; Buscema, M.; Steele, G. A.; Alvarez, J. V.; Zandbergen, H. W.; Palacios, J. J.; Zant, H. S. J. v. d., Isolation and characterization of few-layer black phosphorus. *2D Mater.* **2014,** 1, 025001.
39. Favron, A.; Gaufres, E.; Fossard, F.; Phaneuf-Lheureux, A.-L.; Tang, N. Y. W.; Levesque, P. L.; Loiseau, A.; Leonelli, R.; Francoeur, S.; Martel, R., Photooxidation and quantum confinement effects in exfoliated black phosphorus. *Nat. Mater.* **2015,** 14, 826-832.
40. Vega-Mayoral, V.; Tian, R.; Kelly, A. G.; Griffin, A.; Harvey, A.; Borrelli, M.; Nisi, K.; Backes, C.; Coleman, J. N., Solvent exfoliation stabilizes TiS2 nanosheets against oxidation, facilitating lithium storage applications. *Nanoscale* **2019,** 11, 6206-6216.
41. Rao, R. R.; Raychaudhuri, A. K., Magnetic studies of a mixed antiferromagnetic system Fe1−xNixPS3. *J. Phys. Chem. Solids* **1992,** 53, 577-583.
42. Fragnaud, P.; Prouzet, E.; Brec, R., Structural study of room temperature synthesized nickel thiophosphate a–NiPS3. *J. Mater. Res.* **1992,** 7, 1839-1846.

43. Wildes, A. R.; Simonet, V.; Ressouche, E.; McIntyre, G. J.; Avdeev, M.; Suard, E.; Kimber, S. A. J.; Lançon, D.; Pepe, G.; Moubaraki, B.; Hicks, T. J., Magnetic structure of the quasi-two-dimensional antiferromagnet NiPS3. *Phys. Rev. B* **2015,** 92, 224408.
44. Wildes, A. R.; Simonet, V.; Ressouche, E.; Ballou, R.; McIntyre, G. J., The magnetic properties and structure of the quasi-two-dimensional antiferromagnet CoPS3. *J. Phys.: Cond. Matter* **2017,** 29, 455801.
45. Murayama, C.; Okabe, M.; Urushihara, D.; Asaka, T.; Fukuda, K.; Isobe, M.; Yamamoto, K.; Matsushita, Y., Crystallographic features related to a van der Waals coupling in the layered chalcogenide FePS3. *J. Appl. Phys.* **2016,** 120, 142114.
46. Kuo, C.-T.; Neumann, M.; Balamurugan, K.; Park, H. J.; Kang, S.; Shiu, H. W.; Kang, J. H.; Hong, B. H.; Han, M.; Noh, T. W.; Park, J.-G., Exfoliation and Raman Spectroscopic Fingerprint of Few-Layer NiPS3 Van der Waals Crystals. *Sci. Rep.* **2016,** 6, 20904.
47. Ridings, C.; Warr, G. G.; Andersson, G. G., Composition of the outermost layer and concentration depth profiles of ammonium nitrate ionic liquid surfaces. *Phys. Chem. Chem. Phys.* **2012,** 14, 16088-16095.
48. Nemes-Incze, P.; Osváth, Z.; Kamarás, K.; Biró, L. P., Anomalies in thickness measurements of graphene and few layer graphite crystals by tapping mode atomic force microscopy. *Carbon* **2008,** 46, 1435-1442.
49. Ueberricke, L.; Coleman, J. N.; Backes, C., Robustness of Size Selection and Spectroscopic Size, Thickness and Monolayer Metrics of Liquid-Exfoliated WS2. P*hys. Status Solidi (b)* **2017,** 254, 1700443.
50. Backes, C.; Campi, D.; Szydłowska, B. M.; Synnatschke, K.; Ojala, E.; Rashvand, F.; Harvey, A.; Griffin, A.; Sofer, Z.; Marzari, N.; Coleman, J. N.; O'Regan, D. D., Equipartition of Energy Defines the Size-Thickness Relationship in Liquid-Exfoliated Nanosheets. *ACS Nano* **2019**.
51. Andrea, L.; Konstantinos, K.-A.; Xavier Diez, B.; Alessandro, K.; Emanuele, T.; Nicola Maria, P.; Giovanna De, L.; Loris, G.; Vincenzo, P., Evolution of the size and shape of 2D nanosheets during ultrasonic fragmentation. *2D Mater.* **2017,** 4, 025017.
52. Ogilvie, S. P.; Large, M. J.; O'Mara, M. A.; Lynch, P. J.; Lee, C. L.; King, A. A. K.; Backes, C.; Dalton, A. B., Size selection of liquid-exfoliated 2D nanosheets. *2D Mater.* **2019,** 6, 031002.
53. Backes, C.; Campi, D.; Szydlowska, B. M.; Synnatschke, K.; Ojala, E.; Rashvand, F.; Harvey, A.; Griffin, A.; Sofer, Z.; Marzari, N.; Coleman, J. N.; O'Regan, D. D., Equipartition of Energy Defines the Size–Thickness Relationship in Liquid-Exfoliated Nanosheets. *ACS Nano* **2019,** 13, 7050-7061.
54. Harvey, A.; Backes, C.; Boland, J. B.; He, X.; Griffin, A.; Szydlowska, B.; Gabbett, C.; Donegan, J. F.; Coleman, J. N., Non-resonant light scattering in dispersions of 2D nanosheets. *Nat. Commun.* **2018,** 9, 4553.
55. Yadgarov, L.; Choi, C. L.; Sedova, A.; Cohen, A.; Rosentsveig, R.; Bar-Elli, O.; Oron, D.; Dai, H.; Tenne, R., Dependence of the Absorption and Optical Surface Plasmon Scattering of MoS2 Nanoparticles on Aspect Ratio, Size, and Media. *ACS Nano* **2014,** 8, 3575-3583.
56. Niu, Y.; Gonzalez-Abad, S.; Frisenda, R.; Marauhn, P.; Drüppel, M.; Gant, P.; Schmidt, R.; Taghavi, N.; Barcons, D.; Molina-Mendoza, A.; de Vasconcellos, S.; Bratschitsch, R.; Perez De Lara, D.; Rohlfing, M.; Castellanos-Gomez, A., Thickness-Dependent Differential Reflectance Spectra of Monolayer and Few-Layer MoS2, MoSe2, WS2 and WSe2. *Nanomater.* **2018,** 8, 725.
57. Zhang, C. J.; Pinilla, S.; McEvoy, N.; Cullen, C. P.; Anasori, B.; Long, E.; Park, S.-H.; Seral-Ascaso, A.; Shmeliov, A.; Krishnan, D.; Morant, C.; Liu, X.; Duesberg, G. S.; Gogotsi, Y.; Nicolosi, V., Oxidation Stability of Colloidal Two-Dimensional Titanium Carbides (MXenes). *Chem. Mater.* **2017,** 29, 4848-4856.
58. El-Kemary, M.; Nagy, N.; El-Mehasseb, I., Nickel oxide nanoparticles: Synthesis and spectral studies of interactions with glucose. *Mater. Sci. Semicond. Process.* **2013,** 16, 1747-1752.
59. Newman, R.; Chrenko, R. M., Optical Properties of Nickel Oxide. *Phys. Rev.* **1959,** 114, 1507-1513.
60. Withnall, R.; McCluskey, M.; Andrews, L., Absorption spectra of the phosphorus oxide (PO2 and PO3) radicals in solid argon. *J. Phys. Chem.* **1989,** 93, 126-129.
61. Meingast, L.; Koleśnik-Gray, M.; Siebert, M.; Abellán, G.; Wild, S.; Lloret, V.; Mundloch, U.; Hauke, F.; Hirsch, A.; Krstić, V., Effect of TCNQ Layer Cover on Oxidation Dynamics of Black Phosphorus. P*hys. Status Solidi - RRL* **2018,** 12, 1800179.

62. Chu, J.; Wang, F.; Yin, L.; Lei, L.; Yan, C.; Wang, F.; Wen, Y.; Wang, Z.; Jiang, C.; Feng, L.; Xiong, J.; Li, Y.; He, J., High-Performance Ultraviolet Photodetector Based on a Few-Layered 2D NiPS3 Nanosheet. *Adv. Funct. Mater.* **2017,** 27, 1701342.
63. Filik, J.; Ashton, A. W.; Chang, P. C. Y.; Chater, P. A.; Day, S. J.; Drakopoulos, M.; Gerring, M. W.; Hart, M. L.; Magdysyuk, O. V.; Michalik, S.; Smith, A.; Tang, C. C.; Terrill, N. J.; Wharmby, M. T.; Wilhelm, H., Processing two-dimensional X-ray diffraction and small-angle scattering data in DAWN 2. *J. Appl. Crystallogr.* **2017,** 50, 959-966.

TOC figure

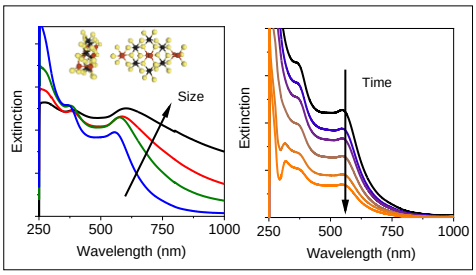
Extinction
Size
250
500
750
1000
Wavelength (nm)
Extinction
Time
250
500
750
1000
Wavelength (nm)